Jinst

PUBLISHED BY IOP PUBLISHING FOR SISSA MEDIALAB

RECEIVED: *June 2, 2025*
REVISED: *July 28, 2025*
ACCEPTED: *September 2, 2025*
PUBLISHED: *October 8, 2025*

TECHNICAL REPORT

Characterization of a DOI-corrected Compton camera system based on LYSO scintillators

---

Changran Geng,[a,b] **Xiaowen Tian**[a] **and Xiaobin Tang**[a,b,*]

[a] *Department of Nuclear Science and Technology, Nanjing University of Aeronautics and Astronautics,*
29 Jiangjun Road, Nanjing, China
[b] *Key Laboratory of Advanced Nuclear Technology and Radiation Protection,*
Ministry of Industry and Information Technology,
Nanjing, China

E-mail: `tangxiaobin@nuaa.edu.cn`

ABSTRACT: The Compton camera reconstructs gamma-ray sources by measuring the energy and interaction positions of scattered photons in the scatterer and absorber layers, based on the Compton scattering formula. In recent years, this technique has attracted attention in medical imaging and nuclear security. A Compton camera has been developed using LYSO scintillators with integrated depth-of-interaction (DOI) correction. LYSO crystals offer high light output, and SiPM readouts enable precise DOI localization. The system comprises scatterer and absorber layers made of LYSO arrays, with SiPMs decoding both interaction positions and energies. Tests using gamma-ray sources demonstrated an energy resolution of around 14%@511 keV and good timing performance. Results show that DOI correction significantly improves spatial resolution and image quality, reducing the full width at half maximum (FWHM) by 5–10 mm and indicating strong potential for applications in medical imaging and nuclear security.

KEYWORDS: Compton imaging; Gamma detectors (scintillators, CZT, HPGe, HgI etc); Radiation monitoring

---

[*] Corresponding author.

https://doi.org/10.1088/1748-0221/20/10/T10004

Contents

1 Introduction

Compton cameras are advanced gamma-ray imaging devices that utilize the principles of Compton scattering to reconstruct the origin of incident photons [1, 2]. By detecting both the scattered photon and the recoil electron resulting from the initial interaction, these cameras can determine the direction and energy of the incoming gamma rays, enabling the visualization of gamma-ray sources. This capability is particularly valuable in fields such as nuclear medicine, astrophysics, and homeland security, where non-invasive and precise imaging is crucial [3–7].

In recent years, the development of Compton camera technology has accelerated, driven by the demand for higher sensitivity, improved spatial resolution, and enhanced energy resolution [8, 9]. These advancements have the potential to transform gamma-ray imaging, offering more accurate detection and localization of radioactive sources. For instance, in medical imaging, Compton cameras can facilitate the simultaneous assessment of multiple radioisotopes, overcoming limitations, e.g. limited efficiency for high energy photons,associated with traditional imaging modalities like Single Photon Emission Computed Tomography (SPECT) and Positron Emission Tomography (PET) [10–13].

Among the various types of Compton cameras, those employing Cadmium Zinc Telluride (CZT) detectors are renowned for their exceptional energy resolution and the advantage of room-temperature operation [14–17]. However, CZT-based systems often suffer from smaller detector sizes, leading to lower detection efficiency and limiting their applicability in scenarios requiring large-area coverage [13, 14, 18, 19].

Alternatively, scintillator-based Compton cameras present several advantages, including high detection efficiency, robust energy resolution, and the flexibility to operate across a broad energy spectrum [20–22]. These features make them particularly suitable for applications demanding high

2025 JINST 20 T10004

sensitivity and low background noise. Nevertheless, challenges persist, such as limited spatial resolution, susceptibility to pile-up effects, and the necessity for complex reconstruction algorithms. Moreover, the use of scintillator materials can introduce noise and uncertainty into the measurements. Despite the issues, many efforts have been made in the field for applying Compton Camera technique in proton therapy, heavy ion therapy and nuclear medicine [23–25].

A significant issue arises when utilizing larger scintillator detectors (with size of several mm), the lack of precise interaction localization can lead to considerable positional uncertainty. In PET applications, this issue has been addressed by pioneering work in 2011, the NIRS group of T. Yamaya published a study on their 'X-tal cube', which employed SiPM readout on all 6 surfaces for DOI correction [26].

In this study, we focus on the development of a scintillator-based Compton camera integrated with Depth of Interaction (DOI) correction technology. By accurately determining the interaction depth within the detector, DOI correction aims to mitigate spatial resolution degradation caused by parallax errors, especially in thick scintillator crystals. We have designed and constructed a prototype system incorporating DOI capabilities and conducted comprehensive performance evaluations under various experimental conditions. Through these enhancements, we aim to expand the applicability of Compton cameras in medical imaging, contributing to advancements in diagnostic and therapeutic procedures that ultimately benefit both clinical practice and research.

2 Materials and methods

2.1 Hardware of the Compton camera system

2.1.1 Scintillator arrays

The Compton camera uses two segmented scintillator layers: a scatter layer and an absorber layer, each built from a 48×48 array of cerium-doped lutetium yttrium oxyorthosilicate (LYSO:Ce) crystals. In the scatter layer, each crystal pixel measures $0.8 \times 0.8 \times 10\,\mathrm{mm}^3$; in the absorber layer each pixel is $0.8 \times 0.8 \times 18\,\mathrm{mm}^3$. LYSO:Ce was chosen for its high density ($\sim 7.15\,\mathrm{g{\cdot}cm^{-3}}$), high light yield ($\sim 2.5 \times 10^4$ photons/MeV) and fast decay ($\sim 40\,\mathrm{ns}$). All crystal surfaces were polished to optical grade to minimize interfacial scatter and maximize light extraction, thereby improving output uniformity and energy resolution. The crystals were procured from Shanghai Epic Crystal.

Adjacent pixels are optically isolated by 0.2 mm thick barium sulfate ($BaSO_4$) layers, which serve as white reflectors to suppress optical crosstalk. A 0.4 mm thick $BaSO_4$ reflector surrounds the outer perimeter of each array. An aluminum foil (0.1 mm thickness) is laminated onto all external faces of each array for mechanical protection. Including the inter-pixel gaps and encapsulation, each scintillator block spans $\approx 50.1 \times 50.1\,\mathrm{mm}^2$ in cross section, with a depth of 10 mm for the scatter layer and 18 mm for the absorber layer, as shown in figure 1.

2.1.2 Photosensor readout and coupling

Each scintillator array is read out on both ends by silicon photomultiplier (SiPM) assemblies. For depth-of-interaction (DOI) correction, the ratio of signal counts detected by the SiPMs at the two ends varies with the interaction depth of gamma-rays in the crystal. A pre-calibrated relationship between this signal ratio and actual DOI is measured during measurements to determine interaction depth, i.e. DOI. The photosensors are ONSEMI J-Series MicroFJ-60035 devices (TOFTEK, Wuxi, China), with an active area of $6.07 \times 6.07\,\mathrm{mm}^2$ (total package $6.13 \times 6.13\,\mathrm{mm}^2$). These SiPMs have a microcell size of 35 µm, a typical dark count rate of approximately 150 kHz at an overvoltage of 5 V, and are operated at a bias voltage of 29.5 V (corresponding to 5 V over the breakdown voltage). Eighty-eight modules (one per end of each array) are constructed by assembling 8×8 SiPMs in a grid with 0.2 mm gaps. The assembled 8×8 SiPM array covers roughly $49.0 \times 49.0\,\mathrm{mm}^2$ of area, closely matching the scintillator face. The 64 anode channels from each SiPM array are read out through an encoded resistive network that compresses them to four corner outputs. This multiplexing reduces the channel count (64:4) while preserving position encoding via an Anger-like logic.

A $50 \times 50 \times 1\,\mathrm{mm}^3$ optical light guide made of transparent polyethylene terephthalate (PET) is placed between each scintillator array and its SiPM assembly. The light guide spreads the scintillation photons over the SiPM array, ensuring that light from each crystal is shared among multiple SiPM pixels. To ensure optimal optical coupling and to avoid air gaps or surface imperfections at the interface, the PET light guide is coupled to the scintillator surface using flexible optical interface pads (EJ-560, Eljen Technology). Gamma-ray interactions in the LYSO produce scintillation light which is transmitted through the PET guide and then detected by the SiPMs on both ends of the block.

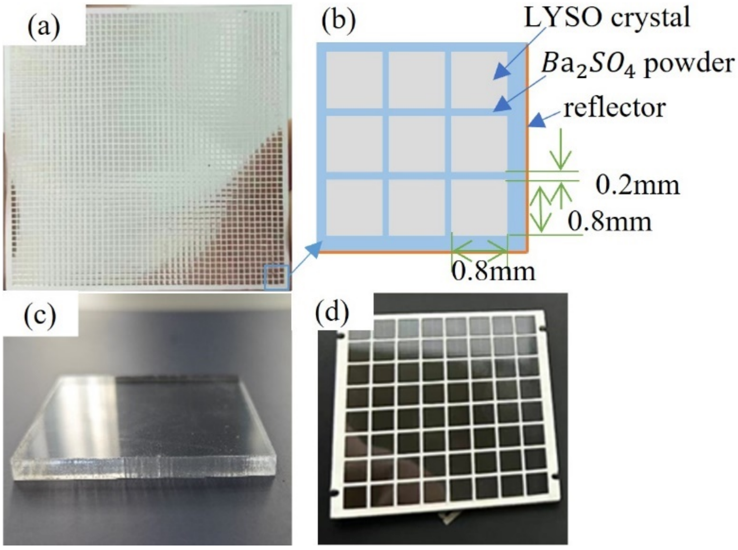

Figure 1. (a) 48×48 scattering layer array, (b) schematic diagram of scintillator array structure, (c) PET light guide, (d) 8×8 SiPM array.

2.1.3 System architecture

The overall structure of the scintillator-based camera is illustrated in figure 2. The position and energy signals from the four compressed output channels are amplified via operational amplifier circuits and then transmitted to an interface board through dedicated coaxial cables. This interface board provides two critical external connections: (1) an Ethernet port linked to the DAQ PC for data transfer, and (2) power supply ports connected to external DC adapters. Subsequently, analog waveforms are digitized by a 12-bit, 125-MS/s Analog-to-Digital Converter (ADC) integrated within the data acquisition (DAQ) card (TOFTEK, Wuxi, China). Energy information is extracted by integrating the digitized waveform, with resolution governed by the ADC's 12-bit dynamic range. Time resolution is

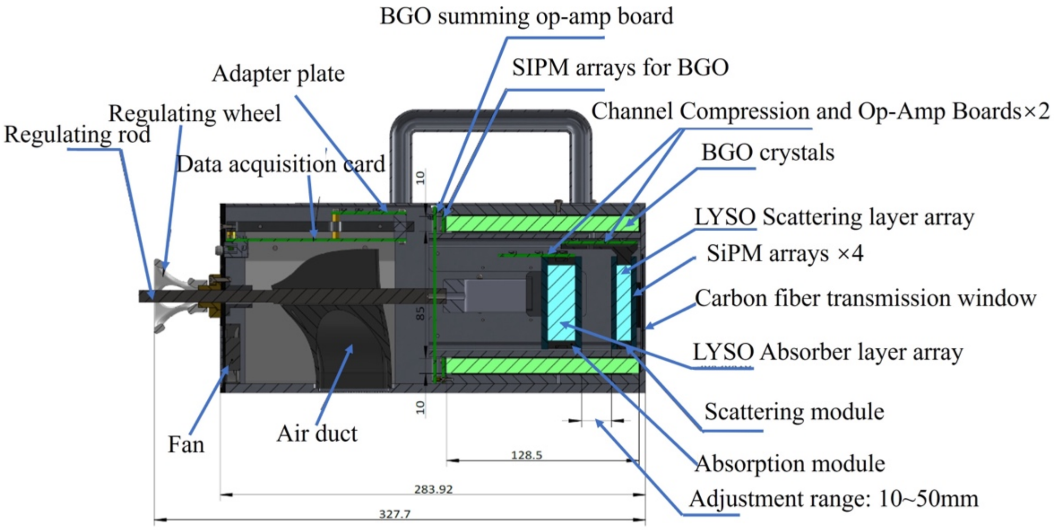

Figure 2. Schematic diagram of the LYSO(Ce) scintillator Compton imaging system.

algorithmically derived via sub-sample interpolation of the ADC waveform, achieving sub-nanosecond precision. This enables the extraction of position, timing, and energy information for each detected event from the ADC-digitized data.

The double-sided readout architecture introduces some passive material — such as PCBs, optical light guides, and mechanical supports — between the scatter and absorber layers. To minimize gamma-ray attenuation and scattering effects, these elements were carefully selected for low-density and low-Z properties, and distributed uniformly. Bulky electronic components such as amplifiers and ADCs were placed outside the photon-sensitive region on dedicated acquisition boards. Signal routing from the SiPM arrays is handled through compact edge connectors and flat flexible cables, avoiding additional bulk in the active volume.

The distance between the scatter and absorber layers of the camera is adjustable within the range of 1 to 5 cm, allowing flexible configuration based on experimental requirements. In the present experiment, the distance between the scatter and absorber layers was fixed at 2.1 cm, with a center-to-center distance of 4.3 cm to ensure efficiency and imaging quality. To suppress background signals in some experimental situations, a BGO-based anti-coincidence veto system is integrated into the camera. The BGO scintillators are rectangular blocks with dimensions of 12.85 cm (length) × 12.6 cm (width) × 1 cm (thickness), mounted around the periphery of the scintillator block. Each BGO unit is optically coupled to a silicon photomultiplier (SiPM) array via a 1 mm thick PET light guide (TOFTEK, Wuxi, China). The BGO veto signals are processed online in the front-end electronics. The analog outputs from the SiPMs are routed to a summing amplifier board, which generates a combined signal that is used to trigger a veto flag in the data acquisition system. The anti-coincidence time window is user-configurable based on experimental situations. In the present study, unless otherwise stated, the veto function was not enabled during the measurements.

2.2 Position decoding and flood map evaluation

Accurate localization within the scintillator array is essential for optimizing the imaging performance of the Compton camera. To address decoding distortions commonly observed near the edges of the detector array, a rectangular decoding method based on the intersection of pixel intensity peaks was adopted in this study to enhance the position reconstruction accuracy.

The decoding procedure consisted of the following steps:Firstly, using Na-22 with an activity of 11.2×10^4 Bq, 61,636,58 events were accumulated, generating the original floodhistogram representing the entire detector array. In this histogram, local maxima in the event count distribution were identified, corresponding to the 48×48 pixels of the scintillator array. Each local peak was associated with a specific physical pixel location within the array. Next, the array was partitioned into rectangular regions based on the locations of these peak intensities. During routine data acquisition, when a new event was detected, the corresponding positional signals derived from the capacitive multiplexing readout circuitry were decoded to obtain the (X, Y) coordinates of the event.

2.3 Energy resolution

Energy resolution is a critical parameter for accurately reconstructing scattering angles and improving the image quality in Compton imaging systems. In this study, the energy spectrum response of the detector system was tested and analyzed using standard gamma-ray sources to extract the energy resolution at characteristic energy peaks. Three gamma sources were employed: a Na-22 source(7.326×10^4 Bq), a Cs-137 source (4.662×10^4 Bq), and a Co-57 source (9.731×10^4 Bq), covering the energy range from 122 keV to 1275 keV. As shown in figure 3, each source was placed between the scatter and absorber layers. The LYSO(Ce) scintillator arrays, using dual-ended readout, simultaneously captured energy signals from both layers. Each data acquisition session was configured with a uniform time windowof 20000 ps was applied to all coincidence events.and lasted for 8 hours to ensure adequate statistics for spectral analysis. The average count rate during calibration was 69.5 kcps. Over a period of 8 consecutive hours of continuous collection, approximately 2 billion events were recorded. The energy distribution of each major peak was fitted with a Gaussian function to extract the full width at half maximum (FWHM).

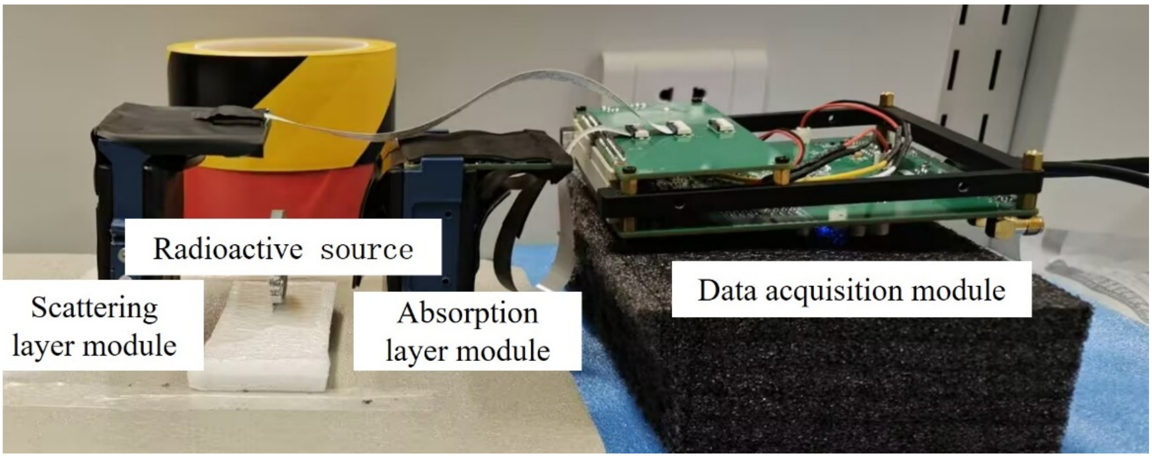

Figure 3. Experimental setup for energy resolution measurement.

2.4 Time resolution

The performance of a Compton imaging system heavily relies on its timing resolution, which determines the ability to distinguish between coincident events and directly affects noise suppression and image quality. In this study, the timing performance of the LYSO(Ce) detector was evaluated using a coincidence time resolution (CTR) measurement based on a Na-22 source as shown in figure 4. Na-22 decays via positron emission and produces two 511 keV annihilation gamma photons emitted nearly simultaneously in opposite directions. This makes it ideal for precise time-difference measurements. The time differences between detector pairs were recorded via the data acquisition system.

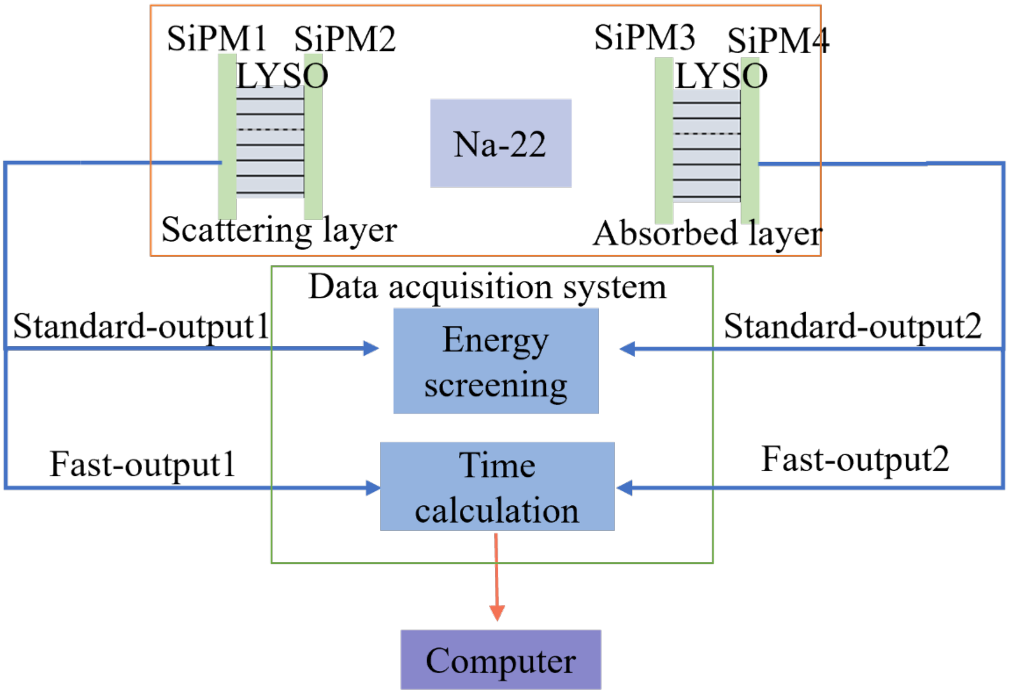

Figure 4. Schematic diagram of time resolution experiment measurement.

2.5 Imaging performance evaluation

The imaging performance of the LYSO(Ce) Compton system was evaluated using a series of F-18 source experiments. These tests were designed to assess event discrimination and image reconstruction under realistic conditions. As shown in figure 5, the experimental setup includes a PTFE imaging mold featuring two cylindrical holes (0.5 cm and 0.25 cm diameter, 3 cm apart) filled with F-18 radiopharmaceutical liquid sources to simulate spatially distributed point sources. Both single-source (1.184×10^6 Bq) and dual-source (1.184×10^6 Bq and 1.036×10^6 Bq) configurations were tested to analyze system performance under varying activity conditions.

3 Results and discussion

3.1 Position decoding and flood map evaluation

The implementation of the 8×8 SiPM array design not only significantly reduced the number of required readout channels, but also simplified the overall system architecture and improved data transmission efficiency. Using the aforementioned encoding method, the outputs from the 8×8 SiPM array were successfully compressed and decoded. Figure 6 presents the position decoding maps

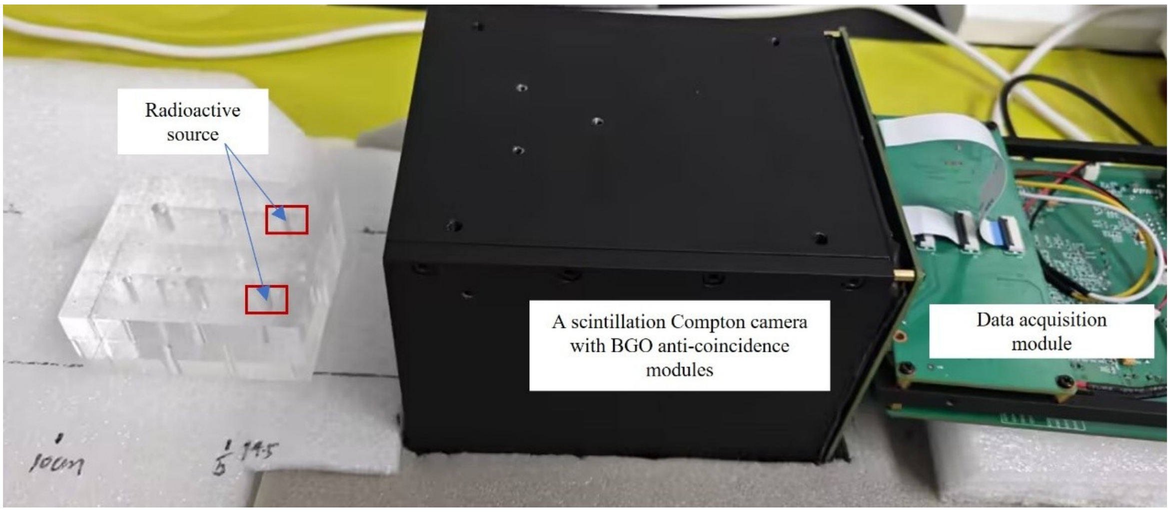

Figure 5. Photograph of the experimental setup for data acquisition using the Compton imaging system and an F-18 radiopharmaceutical source.

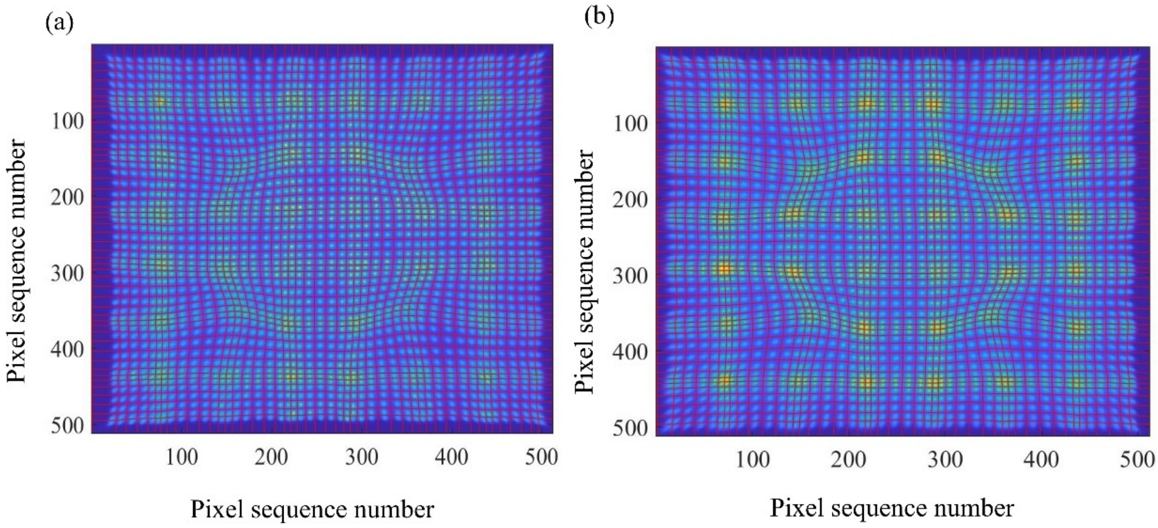

Figure 6. Position decoding diagram of the scattering layer and absorption layer: (a) Position decoding of the scattering layer; (b) Position decoding of the absorption layer.

for both the scatter and absorber layers. By applying the rectangular decoding method, the crystal positions in both layers could be accurately identified. Notably, the decoding performance at the peripheral regions of the array was markedly improved, with enhanced clarity and precision in crystal recognition. This improvement ensures reliable spatial localization across the entire scintillator camera system, thereby supporting high-resolution Compton imaging performance, as shown in figure 6. The raw data is obtained from the detector imaging, and the original count map is a 512 × 512 pixel 2D image representing the detector response area of the entire Compton scattering layer, or the pixel distribution of the reconstructed image. Therefore, the number 512 refers to the “canvas” size of the data matrix. Even though the crystal array consists of 2304 crystal units, the entire array is mapped to a 512 × 512 coordinate space to ensure display and localization accuracy. The image resolution is 512 × 512 pixels, where each element countmap(y, x) represents the number of counts recorded in a specific physical region (pixel) at row y and column x. This matrix is ultimately displayed as a grayscale or pseudocolor image using imagesc(countmap), allowing for the observation of the spatial distribution of signal intensity. The bright regions correspond to areas of high count rates received by the detector, typically consistent with the crystal units where the incident particles are concentrated and penetrate. The dim regions represent areas of lower count rates, which may correspond to gaps between crystals or edge regions. These areas may also exhibit reduced signal intensity due to shielding or angular misalignment.

3.2 Energy resolution

Gamma-ray spectra were recorded from standard sources (^{22}Na,^{57}Co, and^{137}Cs) using dual-end readout for each pixel. The full-energy photopeak of each spectrum was analyzed, and the full width at half maximum (FWHM) was determined. The energy resolution, defined as FWHM divided by peak energy, was calculated accordingly. Results showed a clear energy dependence: higher-energy photopeaks (e.g., 662 keV from^{137}Cs) exhibited narrower FWHM values, corresponding to better energy resolution compared to lower-energy peaks such as the 122 keV line from^{57}Co. At 511 keV, the average energy resolution is 17.91% for the absorber layer and 14.38% for the scatterer layer. Figures 7 display pixel-by-pixel energy resolution maps for the scatter and absorber layers, respectively. The color bar represents the Energy Resolution (%). The darker the color, the smaller the energy resolution. The x-axis corresponds to crystal pixel numbers 1–48, while the y-axis represents crystal pixel numbers 1–48. Figure 8 presents the energy spectra of two central positions and two corner

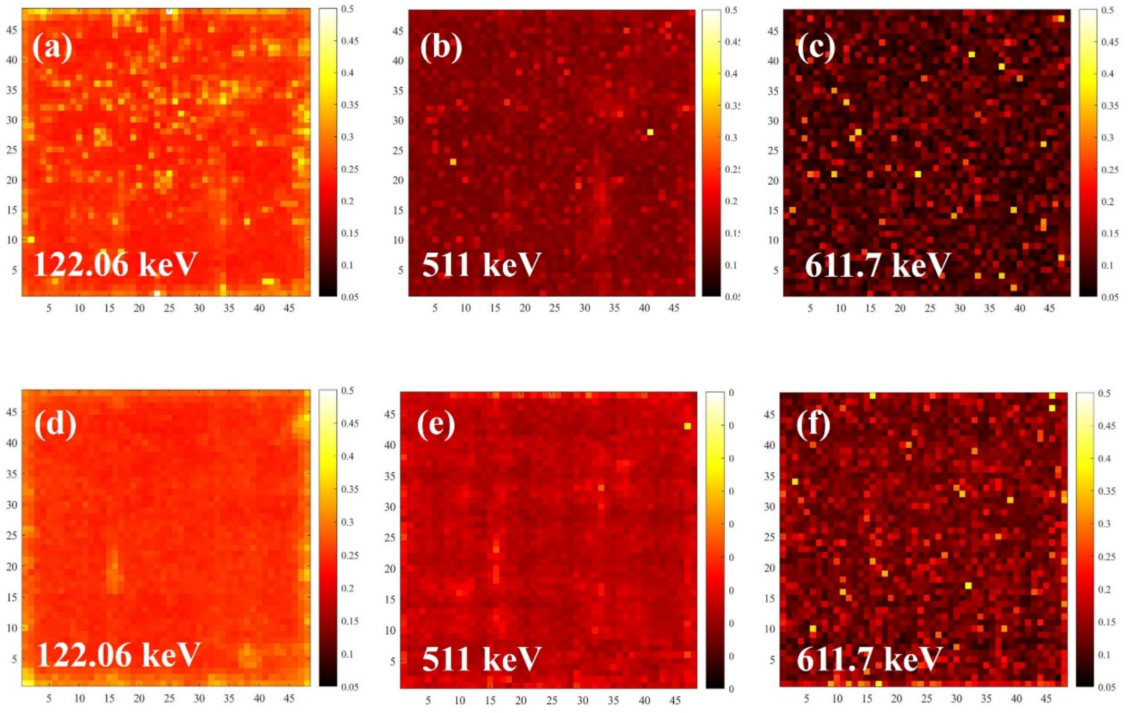

Figure 7. Hotspot map of relative energy resolution of individual pixel crystals in the scattering layer/ the absorption layer.

2025 JINST 20 T10004

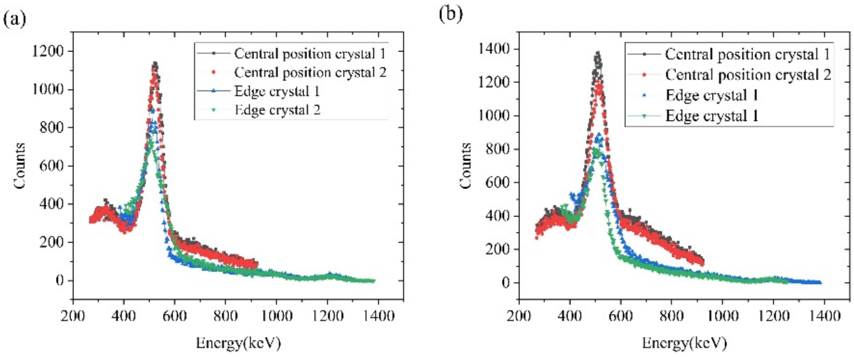

Figure 8. Representative gamma energy spectrum for (a)scatter layer and (b)absorption layer.

positions in both the absorber layer and the scatterer layer. These maps reveal spatial variation in performance across the arrays, with central pixels generally achieving better energy resolution due to more uniform light collection. This is primarily due to optical light transport: scintillation photons generated deeper in the absorber must travel a longer path to the photodetector and undergo greater attenuation and scattering before detection, which degrades the energy resolution. In quantitative terms, the absorber stage's energy resolution was observed to be a few percentage points worse than that of the scatter stage. Additionally, crystals at the detector edges showed worse energy resolution than central crystals, likely due to decoding artifacts and non-uniform light collection at the periphery.

3.3 Time resolution

Coincidence timing performance was characterized by measuring the distribution of time differences between valid coincident events in the scatter and absorber layers. Figure 9(a) shows the histogram of these time differences. The distribution approximates a Gaussian profile and was fitted accordingly, as shown in figure 9(b). The fitted function yielded a full width at half maximum (FWHM) of 3130.80 ps with a standard error of ±23 ps. The narrow width and high consistency of this distribution reflect the stable temporal response of the system, supporting its suitability for coincidence-based Compton

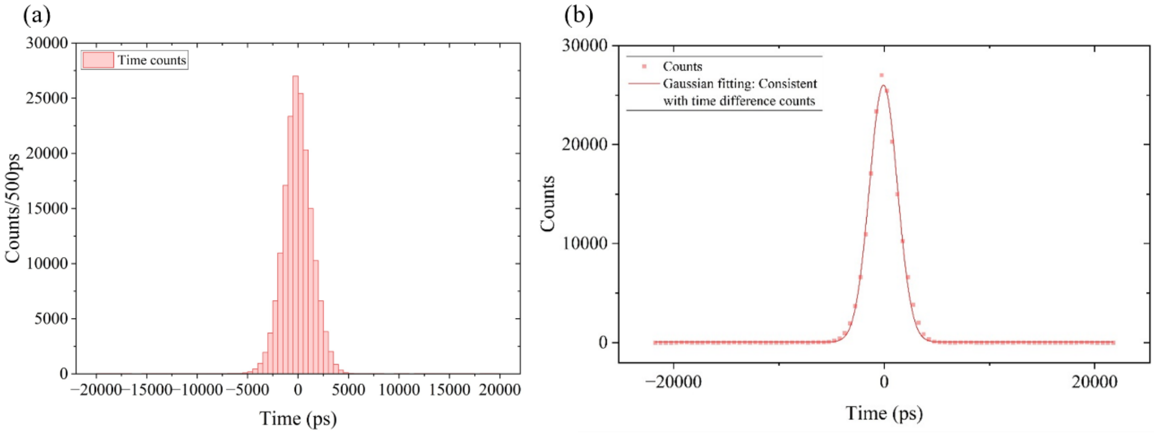

Figure 9. (a) Time difference distribution between scatter and absorber layer of the Compton camera; (b) experimental data points together with Gaussian fit curve.

2025 JINST 20 T10004

imaging. Even the time resolution is not optimal, this performance is primarily attributed to two factors in our experimental setup: transit time spread introduced by the relatively larger scintillator crystals in the dual-end readout configuration (where light propagation time varies with interaction depth), and the use of front-end electronics and data acquisition systems not optimized for ultra-fast timing applications.

3.4 Imaging performance

To evaluate imaging performance,a ^{18}F point source and a dual-source configurationwere reconstructed using both a simple backprojection (SBP) algorithm and a three-dimensional maximum-likelihood expectation-maximization (MLEM) algorithm. Figures 10 and 11 compare reconstructed images with and without depth-of-interaction (DOI) correction.

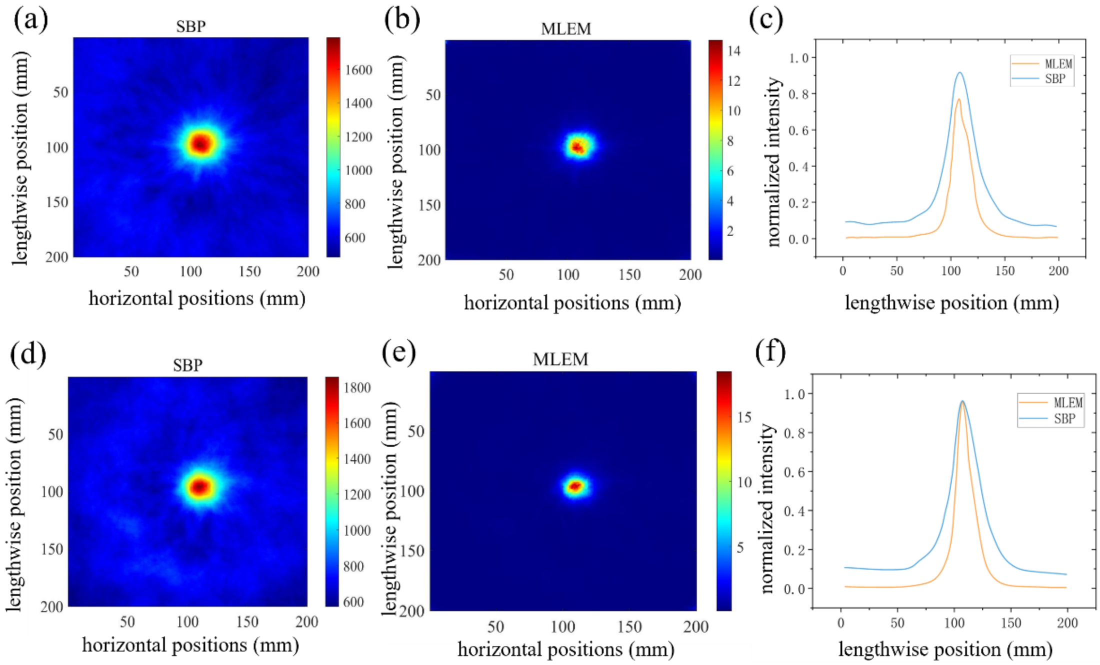

Figure 10. Point source image reconstructions. Left: image reconstruction of a single ^{18}F point source via a simple back projection (SBP) algorithm. Middle: reconstruction of the same source via an iterative MLEM algorithm. Right: x-projections for both image recon- structions. The top row shows the data without, the bottom one with DOI corection.

For the single-source configuration, SBP reconstruction without DOI correction resulted in a spatialFWHM of 32.3 ± 1.54 mm, which was reduced to 26.8 ± 1.08 mm upon applying the DOI correction. The MLEM algorithm further improved spatial resolution: FWHM values were reduced from 18.62 ± 0.31 mm (without DOI) to 13.20 ± 0.16 mm (with DOI).

In the dual-source scenario(3 cm apart), SBP reconstruction without DOI correction produced partially merged peaks with an overall FWHM of 33.63 ± 1.72 mm. After applying DOI correction, the two sources became more clearly distinguishable, and the FWHM was reduced to 25.0 ± 1.63 mm. MLEM reconstructions showed better separation, with FWHMs of 18.3 ± 0.36 mm (without DOI) and 12.0 ± 0.19 mm (with DOI). These findings underscore the critical role of DOI information in enhancing spatial resolution and source discrimination in Compton imaging.

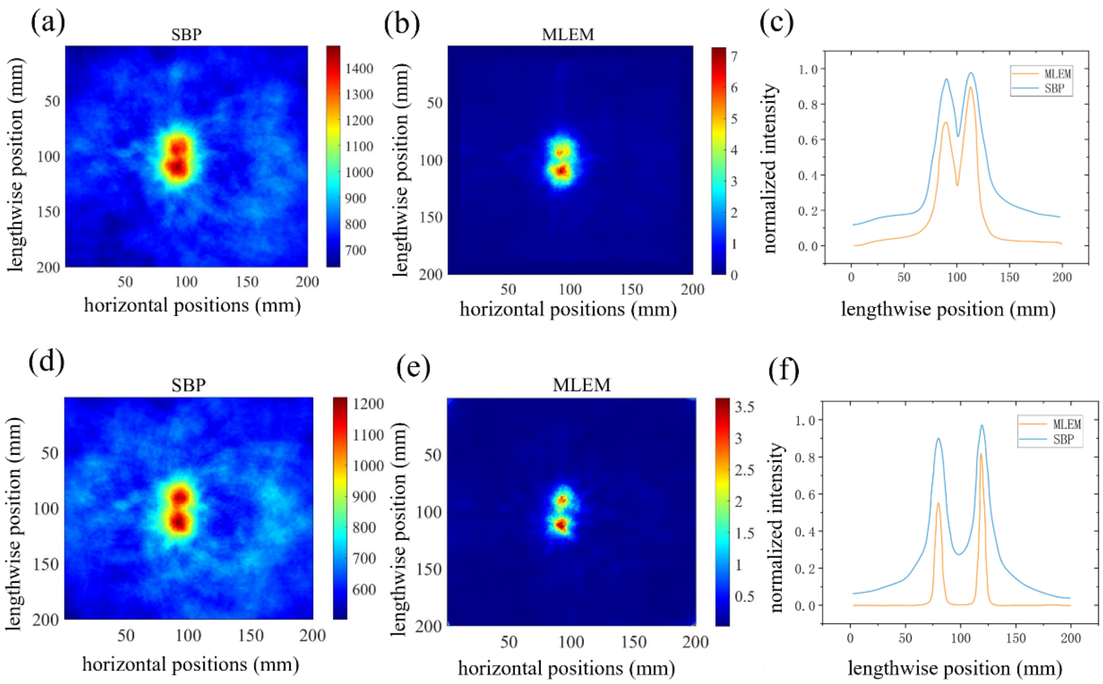

Figure 11. Dual source image reconstruction. Left: image reconstruction of a single ^{18}F point source via a simple back projection (SBP) algorithm. Middle: reconstruction of the same source via an iterative MLEM algorithm. Right: x-projections for both image reconstructions. The top row shows the data without, the bottom one with DOI correction.

Despite these advancements, this study still has some limitations. The testing conditions in this work were relatively limited, and more comprehensive performance tests can be conducted in subsequent studies. As the work focused primarily on medical imaging applications, angular resolution and efficiency were not specifically evaluated under the current experimental framework. Additionally, the energy resolution of the scintillators can be further improved through crystal optimization methods such as special end-face treatment.

4 Conclusion

In this work, we developed a compact Compton camera based on a two-layer scintillation detector system and performed comprehensive experimental evaluations to evaluate its performance. The imaging capabilities, energy resolution, and spatial resolution were systematically tested using various gamma-ray sources. The results demonstrate that the system can effectively reconstruct gamma-ray images and identify source distributions, validating its feasibility for future applications in medical imaging, radiation monitoring, and environmental radioactivity assessment. This study provides a foundation for the continued optimization and deployment of compact Compton imaging systems in practical scenarios.

Acknowledgments

This work is supported in part by the National Natural Science Foundation of China (Grant No. 12220101005), the Natural Science Foundation of Jiangsu Province (Grant No. BK20220132), and the Foundation of Graduate Innovation Center in NUAA (Grant No. xcxjh20230619).

References

[1] M. Fontana et al., *Compton camera study for high efficiency SPECT and benchmark with Anger system*, *Phys. Med. Biol.* **62** (2017) 8794.

[2] J. Kataoka et al., *Handy Compton camera using 3D position-sensitive scintillators coupled with large-area monolithic MPPC arrays*, *Nucl. Instrum. Meth. A* **732** (2013) 403.

[3] R.K. Parajuli, M. Sakai, R. Parajuli and M. Tashiro, *Development and Applications of Compton Camera — A Review*, *Sensors* **22** (2022) 7374.

[4] S. Boggs, *The Advanced Compton Telescope Mission*, *New Astron. Rev.* **50** (2006) 604 [`astro-ph/0608532`].

[5] T. Watanabe et al., *Development of an omnidirectional gamma-ray imaging Compton camera for low-radiation-level environmental monitoring*, *Jap. J. Appl. Phys.* **57** (2017) 026401.

[6] B. Mehadji et al., *$\beta+$ surgical radio-guidance using a small Compton-angles collimation probe*, 2024 *JINST* **19** T08002.

[7] J. Zhu et al., *MeV astrophysical spectroscopic surveyor (MASS): a compton telescope mission concept*, *Exper. Astron.* **57** (2024) 2 [`arXiv:2312.11900`].

[8] M. Kazemi Kozani, *Machine learning approach for proton range verification using real-time prompt gamma imaging with Compton cameras: addressing the total deposited energy information gap*, *Phys. Med. Biol.* **69** (2024) 075019.

[9] Y. Sato, *Identification of depth location of a radiation source by measurement from only one direction using a Compton camera*, *Appl. Radiat. Isot.* **195** (2023) 110739.

[10] M. Pizzichemi et al., *A new method for depth of interaction determination in PET detectors*, *Phys. Med. Biol.* **61** (2016) 4679.

[11] M. Pizzichemi et al., *On light sharing TOF-PET modules with depth of interaction and 157 ps FWHM coincidence time resolution*, *Phys. Med. Biol.* **64** (2019) 155008.

[12] J. Qin, J. Zhao, J. Yu and Y. Wei, *[18F]-NOTA-FAPI-04 PET/CT downgraded the staging of a breast cancer patient and changed their treatment management*, *Precis. Radiat. Oncol.* **8** (2024) 227.

[13] F. Tian et al., *Analysis of influencing factors on the method for determining boron concentration and dose through dual prompt gamma detection*, *Nucl. Sci. Tech.* **32** (2021) 35.

[14] F. Tian et al., *Radiopharmaceutical imaging based on 3D-CZT Compton camera with 3D-printed mouse phantom*, *Phys. Med.* **96** (2022) 140.

[15] S. Hart, P. Jones, L. Pellegri and S. Peterson, *A hybrid CZT-LaBr$_3$:Ce Compton camera system for improving proton therapy imaging*, *J. Phys. Conf. Ser.* **2586** (2023) 012130.

[16] Y. Kim and W. Lee, *Development of a Compton camera based on 3D position-sensitive virtual Frisch-grid CZT detectors*, *Nucl. Instrum. Meth. A* **1053** (2023) 168390.

2025 JINST 20 T10004

[17] J. Caravaca, Y. Huh, G.T. Gullberg and Y. Seo, *Compton and Proximity Imaging of Ac In Vivo With a CZT Gamma Camera: A Proof of Principle With Simulations<sup/>*, IEEE Trans. Radiat. Plasma Med. Sci. **6** (2022) 904.

[18] Z. Hou et al., *Boron concentration prediction from Compton camera image for boron neutron capture therapy based on generative adversarial network*, Appl. Radiat. Isot. **186** (2022) 110302.

[19] R.-Y. Wu et al., *GPU-accelerated three-dimensional reconstruction method of the Compton camera and its application in radionuclide imaging*, Nucl. Sci. Tech. **34** (2023) 52.

[20] N. Koshikawa et al., *High-contrast Compton camera: Challenges to high-quality and broadband imaging*, Appl. Phys. Lett. **125** (2024) 173701.

[21] J. Lee et al., *Development of simultaneous multi-channel data acquisition system for large-area Compton camera (LACC)*, Nucl. Eng. Technol. **55** (2023) 3822.

[22] Z. Yao, Y. Xiao, M. Dong and H. Deng, *Development of a two-layer dense-pixel LYSO Compton camera prototype for prompt gamma imaging*, Phys. Med. Biol. **68** (2023) 045008.

[23] A. Kishimoto et al., *First demonstration of multi-color 3-D in vivo imaging using ultra-compact Compton camera*, Sci. Rep. **7** (2017) 2110.

[24] G. Llosá and M. Rafecas, *Hybrid PET/Compton-camera imaging: an imager for the next generation*, Eur. Phys. J. Plus. **138** (2023) 214.

[25] J.C. Polf et al., *The Effects of Compton Camera Data Acquisition and Readout Timing on PG Imaging for Proton Range Verification*, IEEE Trans. Radiat. Plasma Med. Sci. **6** (2022) 366.

[26] T. Yamaya et al., *A SiPM-based isotropic-3D PET detector X'tal cube with a three-dimensional array of 1 mm^3 crystals*, Phys. Med. Biol. **56** (2011) 6793.